PHYSICAL REVIEW FLUIDS **3**, 103101 (2018)

Three-dimensional steady and oscillatory flow in a double bifurcation airway model

Sahar Jalal, Tristan Van de Moortele,[*] Andras Nemes,[†] Omid Amili, and Filippo Coletti[‡]
Department of Aerospace Engineering and Mechanics, University of Minnesota,
Minneapolis, Minnesota 55455, USA

(Received 5 March 2018; published 10 October 2018)

We investigate the steady expiratory and the oscillatory flow in a planar double bifurcation model with geometric proportions relevant to the respiratory human airways. Expanding on a previous study focused on steady inspiration [Jalal *et al.*, Exp. Fluids **57**, 148 (2016)], we use magnetic resonance velocimetry to characterize the three-dimensional velocity field for a range of Reynolds (Re) and Womersley (Wo) numbers. During expiration the velocity profiles are flatter than in inspiration, due to stronger secondary motions. The latter are characterized by counter-rotating streamwise vortices induced by curvature at the branch junctions. With increasing Re, the vortices gain strength, and for Re $\geqslant$ 1000 they propagate through successive branching generations, profoundly changing the secondary flow pattern. Under oscillatory conditions, as long as the ventilation frequency is in the normal respiration range, the flow topology for both inhalation and exhalation phases is similar to the corresponding steady cases over most of the breathing cycle. On the other hand, in the high-frequency ventilation regime (Wo = 12), the acceleration part of both inhalation and exhalation phases show signature features of oscillatory flows, with high-momentum regions located close to the walls. The phenomenon of counterflow is found to be prominent at Wo $\geqslant$ 6, with reverse flow pockets marking the velocity field especially during the inhalation-exhalation inversion. With increasing oscillation frequency, the secondary motions become more intense during the inhalation phase but are attenuated during the exhalation phase of the cycle. The cycle-averaged drift is found to be significant at low Wo but decreases with increasing ventilation frequency, suggesting that steady streaming is not the main transport mechanism during high-frequency ventilation.

DOI: 10.1103/PhysRevFluids.3.103101

I. INTRODUCTION

Fluid flows in dichotomous branching networks are ubiquitous in biology. The pattern of successively bifurcating vessels is a hallmark of both cardiovascular and respiratory systems in most animals, including humans. Because heart and lung diseases are among the primary cause of death worldwide, the detailed understanding of these type of flows has far-reaching consequences. Moreover, common designs of man-made devices (e.g., heat exchangers, water, and oil piping) replicate this layout, extending the significance of branching networks to various technological settings. Here we focus on an idealized configuration of successive bifurcations, which is explicitly relevant to the anatomy and physiology of the human airways.

---

[*] Current address: Cardiovascular Systems, Inc., St. Paul, Minnesota, USA.

[†] Current address: 4Dx Ltd., Melbourne, Australia.

[‡] fcoletti@umn.edu

The conducting intrathoracic airways allow for the transport of air from the trachea to the bronchi and bronchioles during inhalation, and back to the upper airways during exhalation. (The pulmonary acinus beyond the bronchioles, where the gas exchange takes place, displays profoundly different structure and fluid mechanics [1].) The deeper bronchi grow larger in number but smaller in size, filling the lung volume in a fractal-like manner [2]. Indeed, beyond the morphological complexity and intersubject variability of the human anatomy, the structure of the bronchial tree is remarkably well represented by a system of symmetric bifurcations, with a high level of self-similarity at each branching generation: the daughter-to-mother branch diameter ratio is $h \approx 0.8$, the length-to-diameter ratio of each branch is about 3.5, and the bifurcation angle is $\theta \approx 60-70^\circ$ [3,4]. Such proportions approach the theoretical optimum that minimizes energy expenditure [5–7]. The flow in idealized airway networks respecting these canons has been extensively investigated, using approaches ranging from analytical models to experimental measurements and numerical simulations [4,8–16]. In such models the geometry is highly simplified, with straight and rigid airways of circular cross sections. Even so, the flow is complex and three-dimensional (3D), largely due to secondary (i.e., transverse) motions induced by the curvature at the branching locations, the so-called Dean mechanism [17]. The flow topology is also significantly dependent on the Reynolds number $\mathrm{Re} = Ud/\nu$, where U is the bulk flow velocity, d is the branch diameter of the considered airway, and ν is the fluid viscosity.

The vast majority of past respiratory flow studies have focused on the inhalation phase. Already in his classic review, Pedley [4] wrote: “A disproportionately small amount of work has been done on expiratory flow patterns. It is as if everyone doing a model experiment on inspiration ran out of time or energy when it came to repeating the measurements for expiration.” While the expiratory fluid mechanics has great physiological importance, the trend reported by Pedley has not substantially changed in the last 40 years. The existing experimental studies focused on exhalation were carried out using pointwise or planar techniques, providing valuable but inherently incomplete descriptions of the 3D flow. Schroter and Sudlow [18] used hot wire anemometry and flow visualizations to describe several key aspects of the flow merging from two daughter tubes into a mother tube: these included two pairs of streamwise vortices (manifestation of Dean-type secondary flows) produced at the curved junction between both daughter branches and entering the mother branch. Zhao and Lieber [19] used laser Doppler velocimetry (LDV) and showed that, just downstream of the junction, the streamwise velocity profile along the plane of the bifurcation had two peaks due to the merging of the streams from the daughter branches. These and other studies used single bifurcations and therefore could not address the mutual influence of successive branching generations. This is potentially significant in airway flows due to the relatively short length of each segment. Fresconi and Prasad [14] used particle image velocimetry (PIV) to characterize the secondary flows in a model with three successive planar bifurcations, i.e., with all bifurcation centerlines lying on the same plane. They showed that the local branch geometry determined the velocity field for both inspiratory and expiratory flows, with no visible interplay among adjacent generations. They, however, considered only relatively low flow rates. Recently Jalal *et al.* [15] applied magnetic resonance velocimetry (MRV) to a similar geometry with two successive planar bifurcations. It was demonstrated that the streamwise vortices generated during steady inhalation can in fact propagate through successive bifurcations depending on the Reynolds number (confirming findings from the numerical study of Comer *et al.* [11]). Whether this might happen also during steady exhalation remains an open question.

During the breathing cycle, the alternation of inspiratory and expiratory phases results in an intrinsically time-dependent flow. Depending on the respiration frequency, the velocity fields may significantly differ from those found in steady conditions, especially close to the inversion between inspiratory and expiratory phases [9,20]. The level of unsteadiness is quantified by the Womersely number, i.e., the ratio of the unsteady and viscous forces, $\mathrm{Wo} = a\sqrt{\omega/\nu}$ (where $a = D/2$ is the radius of the branch and ω is the angular frequency of the breathing cycle). If the airways are considered rigid and the respiratory waveform sinusoidal (which are reasonable assumptions for the first several bronchial generations [21]), Re and Wo are sufficient to characterize the oscillatory flow regime in a given geometry. A combination of both parameters, the nondimensional stroke length $L/a = \mathrm{Re}/\mathrm{Wo}^2$ is also commonly used, where L is the average axial displacement of a fluid particle (equal to the stroke volume divided by the local cross-sectional area). Jan *et al.* [9] carried out oscillatory flow experiments in a single bifurcation and mapped the flow behavior over the L/a-Wo^2 space, distinguishing between viscous, unsteady, and convective regimes. In a system of successive bifurcations, the situation is complicated by the fact that Re and Wo vary along the bronchial tree.

Major impulse for investigating various oscillatory regimes has come from the success of high-frequency ventilation (HFV). This is a technique of mechanical ventilatory support routinely used to treat acute lung injury and respiratory distress syndrome, which uses higher-than-normal breathing frequencies and low tidal volumes [22,23]. In HFV the tidal volume is much smaller than the lung dead space (the volume of inhaled air not taking part in the gas exchange), suggesting that transport modalities other than bulk advection are at play. Fredberg [24] first argued this could be explained by an *augmented diffusion* resulting from the interaction between axial convection and radial diffusion, the latter being enhanced by turbulence and secondary motions. However, while the secondary flow strength is expected to increase with Re [13,25], its dependence with Wo is not clear from the literature. For example, the measurements of Peattie and Schwarz [26] indicated weaker secondary flows with increasing Wo, while the simulations of Zhang and Kleinstreuer [20] suggested they are marginally stronger at higher Wo. Beside secondary flows, the fast inversion of flow direction in HFV may produce *counterflow*, i.e., regions where the fluid moves in expiratory direction during inspiratory phases, and vice versa [27–30]. This may have important consequences on the fluid dynamics, as the strong shear destabilizes the flow. Additionally, the different inspiratory and expiratory velocity profiles cause a net drift during each respiration cycle, often referred to as *steady streaming*. This was first identified by Haselton and Scherer [31], and it has since been regarded as one of the key gas exchange mechanisms in HFV [32–34]. However, Bauer *et al.* [29] recently simulated the oscillatory flow in a realistic bronchial tree geometry and concluded that steady streaming plays a minor role in the overall transport.

Simulations of respiratory flows in the upper or central airways are challenging, due to both the geometric complexities and the flow regimes, often turbulent or transitional and with spatially varying Re. Direct numerical simulations and large-eddy simulations provide detailed and reliable insight, but are very computationally expensive and often used for steady flow cases [35–38]. Several studies have used laminar or Reynolds-Averaged Navier-Stokes solvers [11,39,40], but recent high-fidelity simulations suggest that significant unsteadiness persists deep in the bronchial tree [41]. In this scenario, accurate and complete experimental measurements are essential. Volumetric velocimetry techniques have matured in recent years and are increasingly applied to biomedical settings [42]. Specifically, the 3D respiratory flow was investigated by stereo scanning PIV [43], particle tracking velocimetry (PTV) [44], and MRV [15,45]. In the present study, we apply MRV to investigate the steady expiratory and oscillatory flow in a planar double bifurcation airway model. Along with the results for steady inhalation reported in Jalal *et al.* [15], these experiments provide a detailed account of the fundamental flow features characterizing this canonical configuration. Particular emphasis is given to secondary flow structures, their interaction, and spatio-temporal evolution as a function of Re and Wo. The paper is organized as follows. The experimental apparatus and measurement methods are described in Secs. II A and II B, respectively. The results are reported in Sec. III, presenting first the steady exhalation (III A) and then the oscillatory cases (III B). Section IV includes a discussion of the results and the conclusions drawn from them.

II. METHODS

A. Experimental setup and flow regimes

The bifurcation geometry is identical to the one used in the inspiratory flow studies of Comer *et al.* [11] and Jalal *et al.* [15] and approximately follows the anatomic proportions reported by

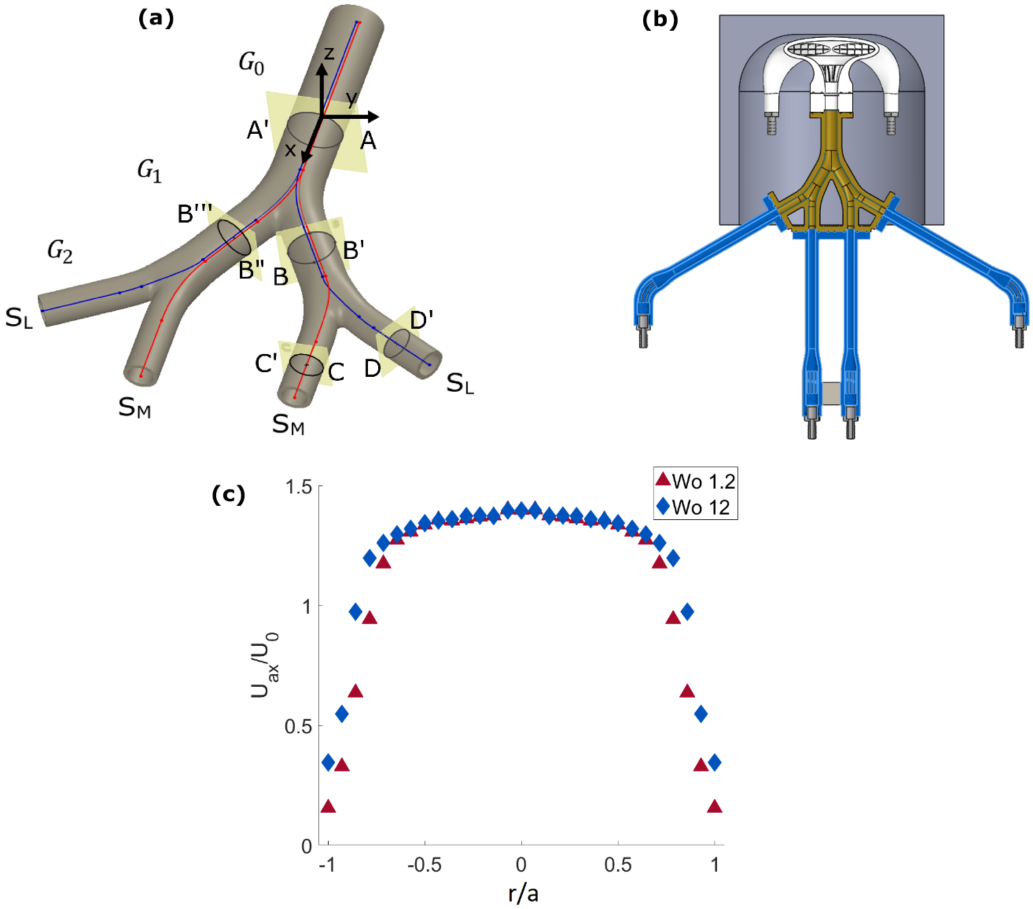

FIG. 1. (a) 3D rendering of the double bifurcation, with cross sections and streamwise abscissas indicated, A-A′, B-B′, C-C′, and D-D′ are at $S/d_0 = 0$, 3.75, 5.3, and 5.3, respectively. (b) CAD model of the bifurcation model (in yellow), with the extension tubes connected at G_2 (in blue), and the upper piece connected to G_0 (in white) fitted into the coil. (c) Azimuthally averaged velocity profile at section A-A′ during peak inhalation for Wo = 1.2 and 12 at peak Re = 2000. The velocity profiles are a somewhat flatter than the theoretical ones for the same Re and Wo due to the very short developmental length.

Weibel [3]. Figure 1(a) shows a sketch of the configuration, whose dimensions are reported in Jalal *et al.* [15]. We label the mother branch as G_0 (zeroth generation), the daughter branches after the first bifurcation as G_1 (first generation), and the granddaughter branches after the second bifurcation as G_2 (second generation). S is the curvilinear abscissa along the centerline, with subscripts M and L indicating medial and lateral paths of G_2, respectively. The centerline is obtained from the bifurcation volume using the software Mimics (Materialise, Belgium) and essentially coincides with the branch axes in the cylindrical portions of the model, and with circular arcs joining successive branches in the bifurcation regions. The abscissa S is used to identify the streamwise location of various cross sections; its origin is taken at a distance $2d_0$ from the first carina (the tip of the bifurcation), $d_0 = 17$ mm being the diameter of the mother branch. At each location in the fluid domain, we define the streamwise or axial velocity U_{ax} as the projection of the velocity vector along the direction tangent to the closest centerline point. The transverse or secondary velocity U_{sec} is the projection of the velocity vector along the plane normal to U_{ax}.

TABLE I. Nondimensional parameters, number of MRV scans, and ranges of relative uncertainty for the investigated cases.

Re	Wo	V_{enc} [m/s]	SNR	No. of scans, N	$\frac{\delta_u}{U_0}$ %
250	–	0.12	154.9	20	1.2–2.5
1000	–	0.25	187.6	14	1.1–2.1
2000	–	0.50	130.6	16	1.6–2.7
4000	–	0.50	70.3	16	1.5–2.6
2000	1.2	0.30	82.4	6	2.2–4.2
2000	3	0.50	62.3	6	5.2–8.7
2000	6	0.50	67.3	6	4.8–8.3
2000	12	0.30	91.5	6	1.5–3

The bifurcation geometry is used to build a physical model [Fig. 1(b)] 3D printed out of Watershed XC 11122 with a wall thickness of about 8 mm. The high-resolution print (25-μm layer thickness) guarantees that the inner walls of the model are hydrodynamically smooth. Figure 1(b) shows a longitudinal cut of the assembly, which includes the main bifurcation piece, four extension tubes connected to the G_2 branches, and an upper piece connected to the G_0 branch. The design is dictated by the need of lodging the bifurcation inside the helmet-shaped coil used for the MRV measurements and then inserting the assembly into the magnet bore. The parts are hermetically flanged together and connected via plastic tubing to the pumping system. This consists of a centrifugal pump (TE-6-MD-SC, Little Giant) for the steady exhalation cases and a custom piston pump for the oscillatory cases. The latter is a modification of the one used in Amili *et al.* [46] and features an aluminum piston sliding through a Plexiglas cylinder (85 mm in diameter) driven by a computer-controlled stepper motor (VXM controller, PK266 motor, Velmex). During the steady exhalation tests, the flow rate is regulated by a digital flow controller (LCR-5LPM-D, Alicat Scientific Inc.) with 2% accuracy. In all tests, four independent valves at the far end of the tubing are adjusted to maintain an equal flow rate through each granddaughter branch, as verified by a ME-6PXL Transonic clamp-on flow meter with 10% accuracy. This choice of boundary condition is aimed at simplifying the analysis, as opposed to a nonuniform flow rate distribution among the distal branches, which would be inherently arbitrary. We remark that imposing a uniform pressure would also result in approximately equal flow rates in all granddaughter branches in steady exhalation at the lowest Reynolds number (for which the local geometry dictates the flow resistance); but this may not be the case at higher Re or in the oscillatory cases. The effect of different boundary conditions is outside the scope of the present study, but it is likely that the medial branches would offer less resistance (and carry more flow), as we showed in steady inspiration [15].

The upper piece attached to the mother branch connects it to the tubing through a lofted honeycomb, limiting unwanted secondary flows that would be caused by the strong bending during the inhalation phase. The arrangement is effective in that the secondary velocity component U_{sec} at the entrance of G_0 is measured to be less than $0.03\,U_{\mathrm{ax}}$. The sudden contraction results in a pluglike inflow, as shown by the streamwise velocity profiles at G_0 close to the peak inhalation phase [Fig. 1(c)]. The G_2 extension tubes also have honeycombs at the bending and are about $16d_2$ long (d_2 being the diameter of the G_2 branch), providing developed inlet flow during exhalation.

We consider steady exhalation cases characterized by outflow Reynolds numbers $\mathrm{Re} = U_0 d_0/\nu$ over the range 250–4000 (Table I), U_0 being the bulk velocity at G_0. This corresponds to regimes spanning from quiet breathing in the subsegmental bronchi to light exertion in the trachea [4]. We also investigate oscillatory cases with $\mathrm{Re} = 2000$ at peak flow rate and Wo (also defined at G_0) between 1.2 and 12. Taking G_0 as the trachea, this corresponds to respiration regimes ranging from sleeping to HFV. (In an adult, $\mathrm{Wo} = 12$ corresponds to a ventilation frequency of approximately 5 Hz, which is in the typical range of clinical HFV applications [34].) We choose a sinusoidal

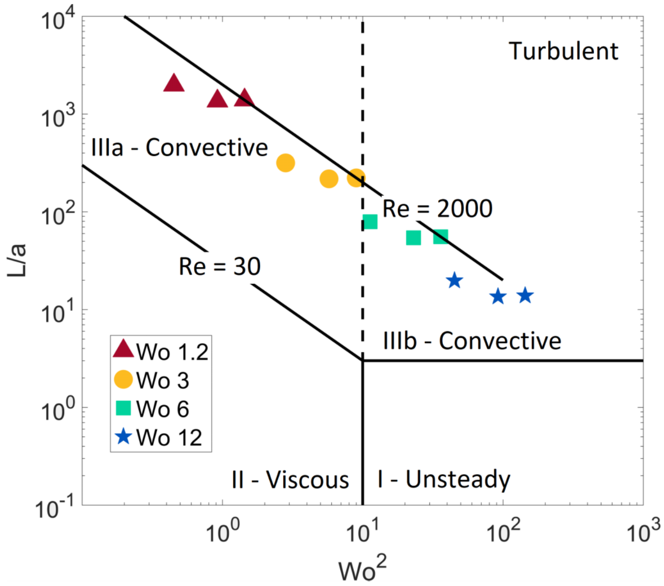

FIG. 2. Position of the considered oscillatory cases in the flow regime diagram proposed by Jan *et al.* [9].

waveform for simplicity [13,47,48] and in consideration of the relatively modest impact of the waveform shapes [28].

For a symmetric divide of the flow rate at each bifurcation, the local Reynolds number at generation G_{i+1} is a factor $2h$ smaller than at G_i (with $h = d_{i+1}/d_i$), and the local Womersley number is a factor h smaller. Therefore, for a given flow setting, the regime may evolve significantly along the branching tree [9,28,48]. In the present model h is ≈ 0.8 for the G_0-G_1 bifurcation and ≈ 0.7 for the G_1-G_2 bifurcation [11,15], both within the anatomical range for human airways [3,49,50]. Figure 2 displays the position corresponding to each generation in the L/a-Wo^2 parameter space for the four oscillatory cases investigated here, along with the regime classification proposed by Jan *et al.* [9]. The cases at Wo = 1.2 and 3 are in “zone IIIa,” where the convective acceleration term of the momentum transport has leading importance and the viscous term has subdominant influence. The cases with Wo = 6 and 12 are in “zone IIIb,” where the convective acceleration has leading importance and the unsteady acceleration has subdominant influence. According to this classification, the first two cases are expected to exhibit quasisteady behavior, and the other two be more strongly time dependent. For all cases, the flow in the G_0 branch lies in the “turbulent” region of the convective zone, although the latter classification was based on dated results [4], and, to our best knowledge, it never received direct verification. The present MRV approach does not measure instantaneous velocities nor Reynolds stresses, and therefore the question of whether turbulent fluctuations occur is not addressed here.

B. Magnetic resonance velocimetry

A 3T Siemens scanner for clinical MRI (magnetic resonance imaging) is used to obtain 3D, three-component velocities on a uniform Cartesian grid with 0.6 mm resolution, using the signaling sequence from Markl *et al.* [51]. For the steady exhalation cases, the data acquisition procedure and the sequence parameters are the same as in Jalal *et al.* [15]. For the oscillatory cases, the phase-resolved velocity is obtained by gating the MRI signal with a procedure similar to the one used by Banko *et al.* [48]. The sinusoidal waveform (corresponding to one respiration cycle) is divided into n time increments referred to as phases. The length of each phase defines the temporal resolution (in a phase-locked average sense) of the measurement, the velocity fields being averaged over each phase. In MRI the information is acquired in the spatial frequency domain (k space) and converted to physical space via inverse Fourier transformation. During each respiration cycle, only information relative to a specific region of k space is acquired. This is repeated until k space is filled, at the spatial frequency resolution corresponding to the desired resolution in physical space. As a trade-off between accuracy and measurement time, we choose $n = 18$ for Wo = 12 and $n = 10$ for the lower Wo cases. Each scan lasts between 20 and 30 min.

For Reynolds numbers between 1000 and 4000, the working fluid is water. For Re = 250 a mixture of water and glycerin (23% in volume) is used, mildly attenuating the MRI signal but ensuring the fluid velocity remains well above the noise floor (less than 1 cm/s). In all experiments we add 0.06 mol/liter of $CuSO_4$, which boosts the signal-to-noise ratio (SNR) without appreciably altering the fluid properties. For each case, N scans are acquired and averaged, increasing the SNR by a factor $\sqrt{N}$ [52]. The value of N is chosen as a trade-off between accuracy and total scan duration (Table I). "Flow-off" scans (performed with the same acquisition parameters but at zero flow rate) generate velocity fields that are subtracted from the raw data, removing potential bias errors associated with inhomogeneities of the magnetic field. The expected uncertainty in the MRV measurements, listed in Table I, is estimated following Pelc *et al.* [53]:

$$\delta_u = \frac{\sqrt{2}\, V_{\mathrm{enc}}}{\pi\, SNR}. \tag{1}$$

SNR is defined as the ratio of the average signal in the fluid over the standard deviation of the signal in the background, and the encoding velocity V_{enc} coincides with the maximum measurable velocity prescribed for each scan. Because of the highly 3D nature of the flow in the bifurcation, the same value of V_{enc} is applied in all three directions. Errors can be significantly larger close to the wall, due to the possibility that a voxel intersects a solid boundary (partial volume effect). This is partly mitigated by masking the domain with a threshold based on the signal magnitude. An outlier detection method is applied based on the local normalized median of velocities, and rejected vectors are replaced with the median of the neighboring vectors. For further details on the postprocessing, the reader is referred to Jalal *et al.* [15].

Some limitations of MRV are worth remarking. The technique has limited accuracy in the immediate vicinity of the wall due to the above-mentioned partial volume effect. Moreover, the noise floor is dependent on the details of the system (SNR, V_{enc}, but also hardware and software components). The former issue does not affect the conclusion drawn from the present study since we do not attempt the analysis of the near-wall dynamics (for example through wall shear stresses). The latter is coped with by adjusting the fluid viscosity as described below, but it does limit the range of attainable regimes.

Figure 3 shows the flow rate measured by integrating the MRV velocity field over the cross section A-A′. The scatter around the imposed sinusoidal waveform are attributed to: MRV uncertainty, including partial-volume effect, averaging of the time-varying flow field over each phase, and small compliance of the plastic tubing connecting the pump and the bifurcation model, possibly causing some phase shift.

III. RESULTS

For clarity of the illustrations and given the symmetric nature of the flow, some of the measured quantities will be shown only in one half or one quarter of the fluid domain. The velocity fields were indeed verified to be symmetric within experimental uncertainty.

A. Steady exhalation

1. *Streamwise velocity*

We first focus on the streamwise velocity fields responsible for the bulk advective transport. Figure 4 shows contours of the velocity magnitude along the plane of the bifurcation [x-y plane

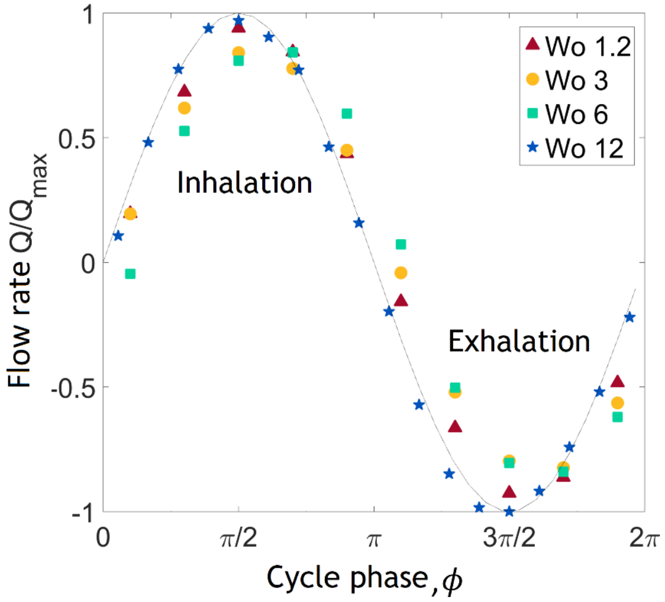

FIG. 3. Measured flow rate at each phase for all Womersley numbers plotted against the theoretical waveform.

in Fig. 1(a)] for the cases Re = 250 and 2000, the latter displaying qualitatively similar behavior as Re = 1000 and 4000. The flow streams from G_2 towards G_0, merging after each junction. As the streams from G_{2L} and G_{2M} merge, a high-momentum region is created at the center of G_1, flanked by low-momentum regions near the wall. At Re = 250 the velocity gradients in G_1 are relatively mild, while at Re = 2000 the high momentum of both streams leads to a jetlike merging with sharp jumps in velocity magnitude. This is also illustrated by B-B′ section, which shows that the

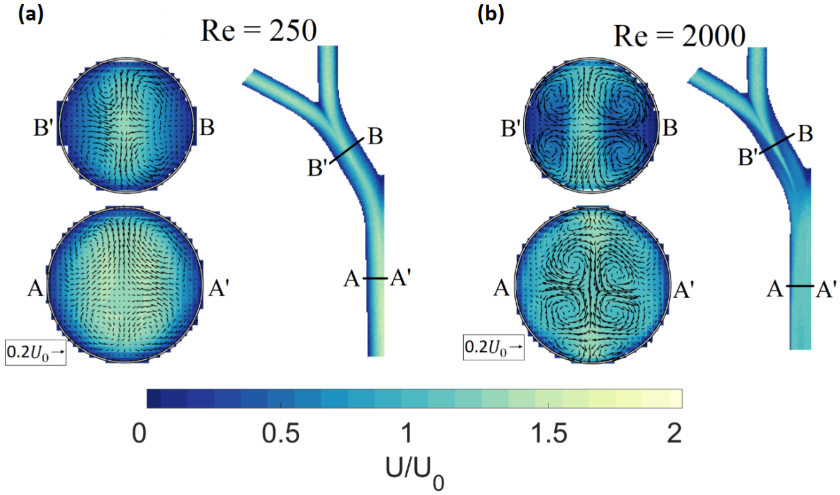

FIG. 4. Contours of velocity magnitude along the bifurcation plane and streamwise velocity along cross sections A-A′ and B-B′, for steady exhalation at Re = 250 (a) and Re = 2000 (b). Secondary flow vectors are shown in the cross sections. A reference velocity vector is shown at the bottom left.

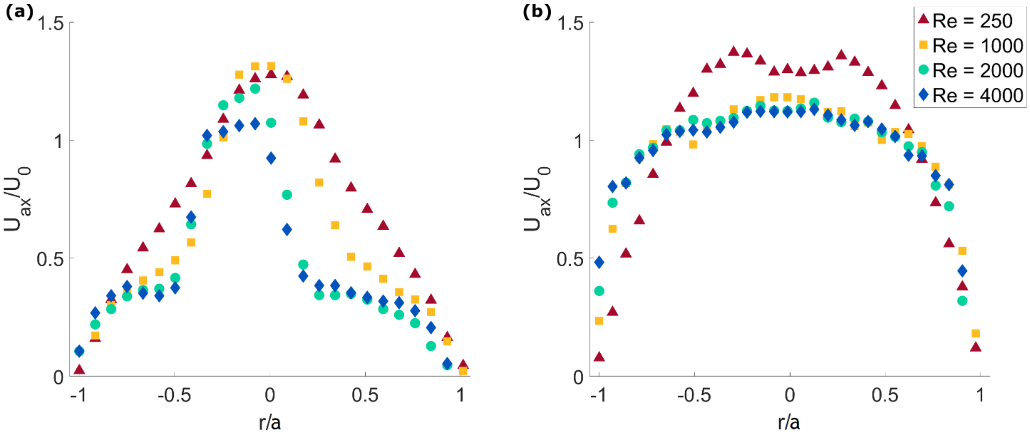

FIG. 5. Streamwise velocity profiles under steady exhalation for all considered Reynolds numbers, at stations (a) B-B′ and (b) A-A′.

high-velocity region extends across the entire branch in the direction normal to the bifurcation plane. Secondary velocity vectors are also displayed, highlighting streamwise vortices whose structure and propagation will be addressed in Sec. III A 2.

Figure 5 shows the streamwise velocity profiles along the bifurcation plane in G_1 and G_0 (stations B-B′ and A-A′, respectively). At G_1 [Fig. 5(a)] the profile for $\mathrm{Re} = 250$ is fairly symmetric around the branch centerline, reflecting the symmetry of the local geometry, and the increase in velocity from the wall to the center of the branch is gradual. For higher Re, as mentioned above, the fast central region contrasts with the slower fluid near the walls, a feature also noted by Lieber and Zhao [8] in their classic single bifurcation study. However, the mutual impact of the successive bifurcations is evident in the asymmetry of the profiles at B-B′ for $\mathrm{Re} = 2000$ and $\mathrm{Re} = 4000$, which are influenced by the downstream turn at the G_1-G_0 junction. At G_0 [Fig. 5(b)] the velocity profile for $\mathrm{Re} = 250$ displays two peaks, resulting from the merging of the two pointy profiles from the daughter branches. For $\mathrm{Re} \geqslant 1000$, the distribution flattens due to the strong secondary velocities pushing the fluid away from the center of the branch. This is in contrast with the $\mathrm{Re} = 250$ case, where the secondary flows have opposite sense of rotation (as discussed below). Turbulent or unsteady transport is also likely to play a role in blunting the profile at the higher Re, but this is not quantified here.

To characterize the degree of streamwise velocity variation within each cross section, we calculate the momentum distortion parameter D [15,45,54]:

$$D = \frac{\int_A (U_{\mathrm{ax}})^2 dA}{Q^2/A} - 1, \tag{2}$$

where A is the cross section area and Q is the local volumetric flow rate. It represents the relative difference of axial momentum with respect to a uniform flow with the same Q. D is a measure of mean longitudinal dispersion, related to the amount of axial strain experienced by the fluid at each cross section due to the mean velocity profile. For reference, fully developed laminar and turbulent pipe flows have values of $D = 0.33$ and $D = 0.02$, respectively. Figure 6 shows D as a function of the streamwise abscissa for the various Re, averaged between the medial and lateral paths (which were negligibly different). We report only the results within the straight branches since the streamwise components in the carinal regions are not trivial to identify univocally. At G_2, D is around the theoretical value 0.33 for the lower Re cases (supposedly laminar and fully developed), while at higher Re the profiles are flatter and D decreases accordingly. At G_1, D remains relatively high for $\mathrm{Re} = 250$, reflecting the pointy shape of the velocity distribution, and is almost

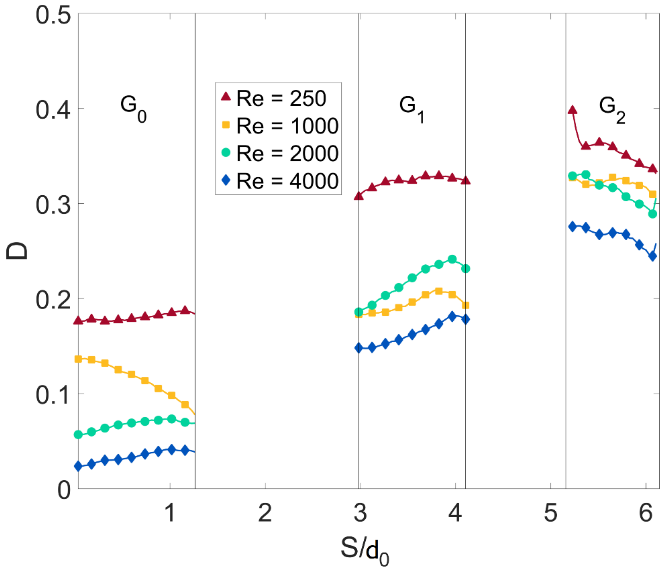

FIG. 6. Momentum distortion parameter D [Eq. (2)] under steady exhalation for all considered Reynolds numbers. The flow direction is towards smaller values of the abscissa.

constant throughout the branch. With increasing Re, because of strong secondary flows spreading the momentum over the cross section, D decreases and tends to drop along the branch. By G_0, the value of D for $\mathrm{Re} = 4000$ is close to the expected value for fully developed turbulent pipe flow. Overall, D has lower values compared to the inspiratory case for the same Reynolds numbers (see Fig. 8 in Jalal *et al.* [15]), indicating generally flatter profiles [4].

2. *Secondary flows*

The cross sections in Fig. 4 indicate the presence of coherent secondary flow structures. In G_1, these are locally generated by the Dean mechanism: at the G_1-G_2 junction, the low-momentum fluid far from the bifurcation plane experiences a transverse pressure gradient stronger than the centrifugal force and is pushed toward the center of curvature of the centerline. This creates two counter-rotating streamwise vortices from each granddaughter branch (lateral and medial), resulting in a system of four vortices. While the flow topology in G_1 is similar for all cases, significant differences are evident at G_0 depending on Re. To localize the streamwise vortices we utilize the vortex identifier Γ_2, a scalar quantity defined at any point P [55]:

$$\Gamma_2(P) = \frac{1}{N}\sum_{i=1}^{N}\frac{[PM \times (U_M - \widetilde{U_P})]\cdot z_P}{\|PM\|\cdot\|U_M - \widetilde{U_P}\|}\,dA, \tag{3}$$

where dA is the area of the interrogation window centered on P, N is the number of points M inside the window, and z_P is the unit vector normal to the measurement plane. U_M is the velocity vector evaluated at each point M, PM is the vector from P to M, and $\widetilde{U_P} = \frac{1}{N}\sum_{i=1}^{N} U\,dA$ is the local convection velocity around P. We choose the radius of interrogation to be 2 voxels (as in Jalal *et al.* [15]), where more details on the vortex identification process are given). Γ_2 has the same sign as the local streamwise vorticity, but it is more effective at locating rotation-dominated regions over shear-dominated region [15]. Visual inspection indicates that, for the present data, this method outperforms other vortex identification methods used by the turbulence community such as the Q criterion [56]. This is likely due to the large size of the vortices, compared to the intense and

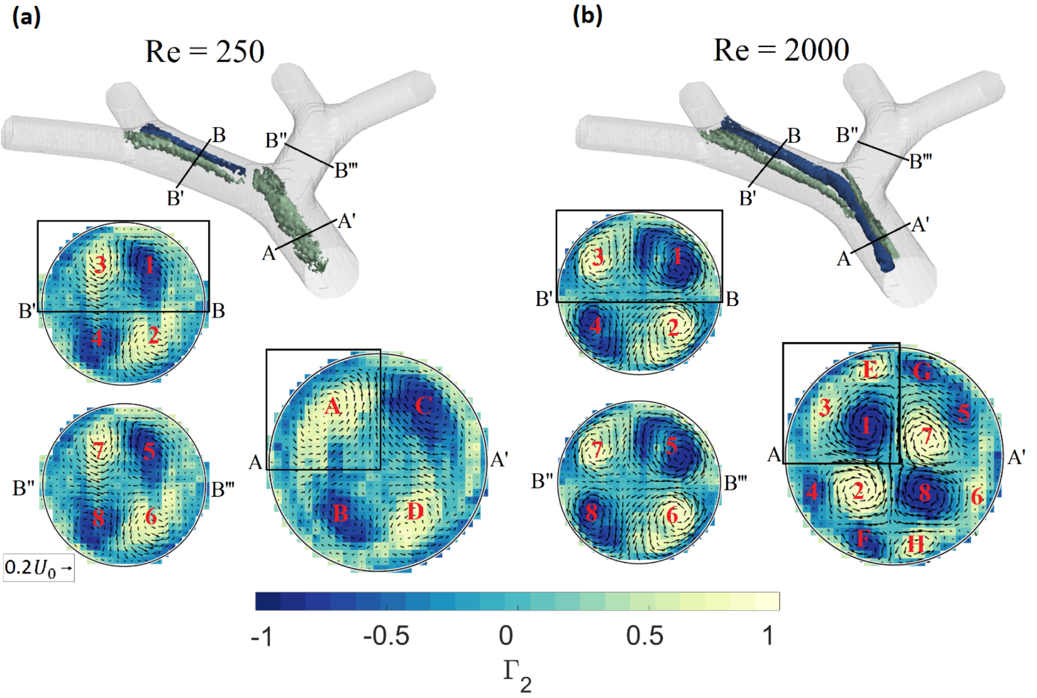

FIG. 7. Isosurfaces of positive (light color) and negative (dark color) Γ_2 [Eq. (3)] identifying vortical structures, and contour maps of Γ_2 with secondary flow vectors at various cross sections for steady exhalation at Re = 250 (a) and Re = 2000 (b). The isosurfaces are only shown in the part of the domain boxed in the cross sections.

localized structures typically highlighted in fully developed turbulence. A systematic comparison of different vortex detection methods is outside the scope of this study.

In Figure 7 we contrast the cases Re = 250 and 2000, which exemplifies the Reynolds number effects on the secondary flow patterns. Isosurfaces of $\Gamma_2 = \pm 0.6$ are shown (comparable to the level of $2/\pi$ adopted by Graftieaux *et al.* [55]), as well as cross-sectional contour plots. For clarity, we show only isosurfaces over the regions highlighted in the cross sections. For both Re, we identify the four counter-rotating vortices in G_1 (labeled 1 through 4 at station B-B$'$ and 5 through 8 at B$''$-B$'''$). At Re = 250 these dissipate before the G_1-G_0 junction, where the Dean mechanism leads to the formation of a similar system of four counter-rotating vortices (labeled A through D) that propagate through the mother branch. At Re = 2000, on the other hand, the vortices formed in G_1 are strong enough to survive into G_0. In particular, vortices 1-2 and 7-8 gain strength thanks to mutual interaction and form a quadruplet of intense counter-rotating vortices visible in the core of G_0. This system of eight vortices is bordered on the upper and lower side by four newly formed structures (labeled E through H). These appear to be generated by the interaction of the four core vortices (1-2-7-8) with the fluid layer between them and the upper or lower side of the branch perimeter.

In order to quantify the strength of the vortical structures, we evaluate their circulation and its evolution along the streamwise abscissa. At each cross section, the circulation Γ for each streamwise vortex is calculated as

$$\Gamma = \int_{A_{\mathrm{VORT}}} \omega_{\mathrm{sec}}\, dA, \tag{4}$$

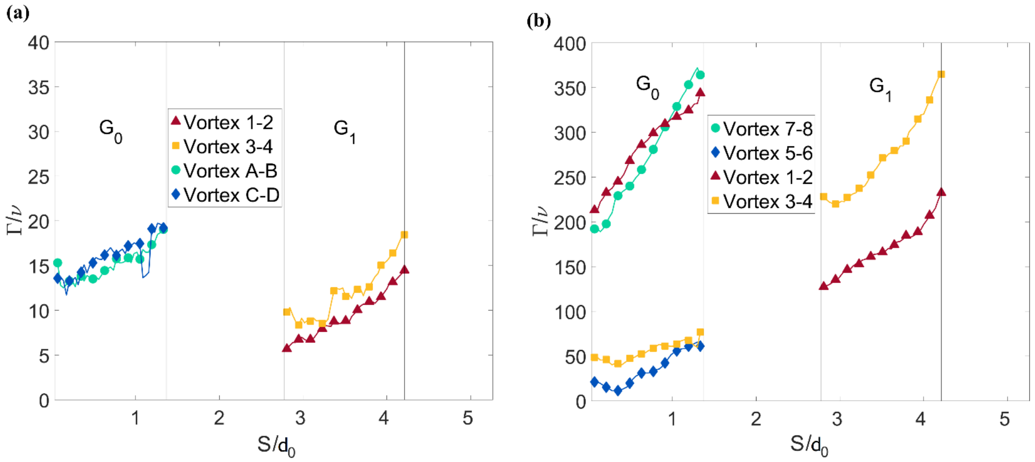

FIG. 8. Normalized circulation Γ [Eq. (4)] of the streamwise vortices in steady exhalation at (a) Re = 250 and (b) Re = 2000. The flow direction is towards smaller values of the abscissa.

where the vorticity ω_{sec} is the curl of the secondary velocity (obtained via a second-order central difference scheme), and the area of the structure A_{VORT} is the area of the detected vortex core using the Γ_2 threshold. In Fig. 8 we use top-bottom symmetry and plot the average circulation for pairs of mirrored vortices (1-2, 3-4, 5-6, and 7-8) normalized by the fluid viscosity. Γ/ν is essentially a Reynolds number based on the characteristic vortex size and rotational velocity. At Re = 250 [Fig. 8(a)] the vortex pairs on the left and right sides of each cross sections have similar strength, confirming that the local bifurcation geometry (which is left-right symmetric) determines the flow features at this low Re. These vortices dissipate along G_1; the newly created ones in G_0 have comparable circulation but undergo a somewhat milder streamwise decay, possibly because the larger branch provides less confinement. As expected, at Re = 2000 [Fig. 8(b)] the circulation levels in G_1 are an order of magnitude higher than the ones at Re = 250. The nonlocal geometry effects are also significant and show their footprint already at the beginning of G_1: vortices 3-4 are sizably more intense than 1-2, being affected by the later turn into G_0. As they penetrate the branch, their circulation diffuses rapidly but both pairs remain strong enough to propagate into G_0. There, vortices 1-2 become stronger than 3-4 due to the mutual interaction with the twin pair 7-8. Vortices 3-4 instead are squeezed along the lateral side of the branch and loose strength [see cross section A-A′ in Fig. 7(b)]. Comparing all Re cases it appears that, for the present bifurcation geometry, streamwise vortices that reach the junction with a normalized circulation above $\Gamma/\nu \approx 100$ propagate through it and into the downstream branch. This is not proposed as a criterion but rather as an indication. It is consistent with the inspiratory flow results of Jalal *et al.* [15], in which only vortices that arrived at the bifurcation with circulation above $\Gamma/\nu \approx 50$ survived to the next generation [see their Fig. 13, where the lower limit appears to be $\Gamma/(U_0 d_0) \approx 0.1$ for Re = 500].

B. Oscillatory flow

1. Streamwise velocity

We analyze here the flow features in the case of an imposed ventilation frequency and contrast them with steady inhalation and exhalation. Figure 9 shows contours of velocity magnitude along the bifurcation plane at Wo = 1.2 for 10 successive phases within the breathing cycle. After an initial period in which the velocity is uniformly small (around the exhalation and inhalation inversion), the flow field shapes up to resemble the steady inhalation flow pattern observed by Jalal *et al.* [15]. The signature feature is the skewed velocity profile in G_1, with high-momentum fluid along the inner side of the bifurcation and slow fluid along the outer walls. We note that the boundary conditions are

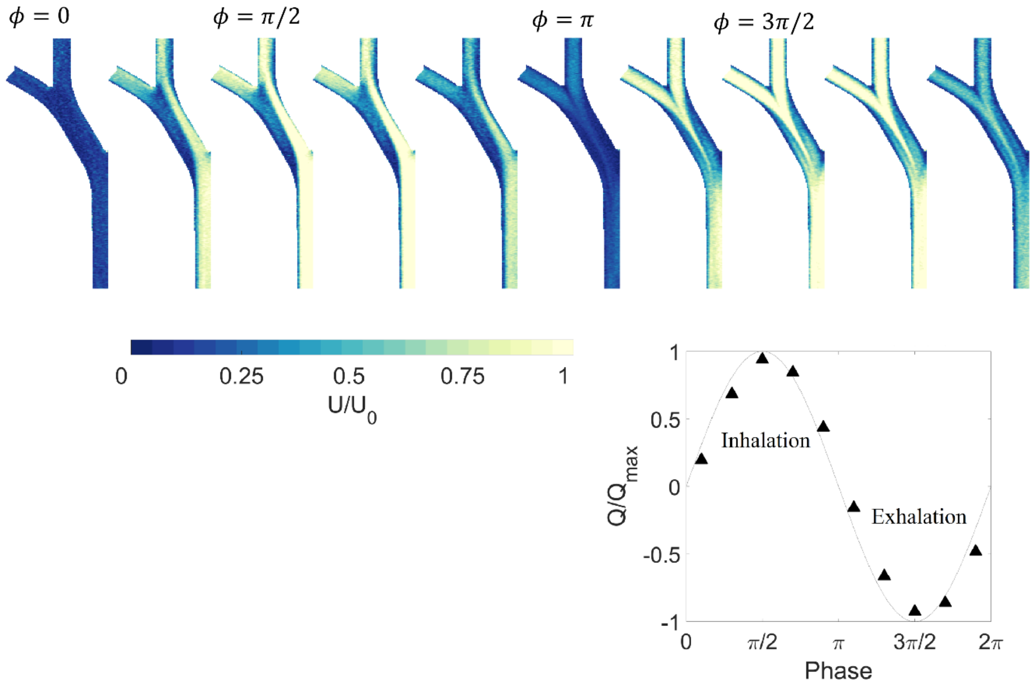

FIG. 9. Contours of velocity magnitude along the bifurcation plane at Wo = 1.2 and peak Re = 2000 during the breathing cycle. The corresponding phase within the oscillatory cycle is labeled above the corresponding contour plots and by the flow rate diagram on the bottom right.

different with respect to Jalal *et al.* [15]: here the four G_2 branches have equal flow rates, while in the steady inhalation study they had equal outlet pressure; still the similarity is remarkable. During inhalation, the velocity field is modulated in magnitude by the time-varying inflow, but essentially maintains the same spatial distribution. This is true also during exhalation, where again the flow closely resembles the respective steady condition (see Fig. 4). The main feature is the jetting from the G_2 branches that merge to create a sharp high-momentum region in G_1, propagating almost into G_0. Very similar observations can be made for Wo = 3 and Wo = 6 (not shown).

Figure 10 displays velocity distributions for Wo = 12, at 10 out of the 18 reconstructed phases in the cycle. At the beginning of inhalation, the velocity magnitude tends to be higher close to the wall than at the center of the branches. This is due to a phase lag between the core flow and the boundary layer and is a signature feature during the inversion phase of high-frequency oscillatory flows [27,28,30,57]. During the first part of inhalation (referred to as the acceleration part, during which the flow rate increases with time), the velocity magnitude is fairly homogeneous except for slower regions close to the carinas. In the second part of inhalation (deceleration), the flow assumes the characteristic topology found in steady conditions, with high or low momentum fluid on the internal or external side of the G_1 branches [15]. At the inversion between inhalation and exhalation, the flow is again faster along the walls than in the branch core. This is followed by a phase in which the velocity magnitude is almost homogeneous. Then, during the deceleration part of exhalation, the flow from G_{2M} and G_{2L} becomes jetlike and merges into G_1, following the pattern seen in steady exhalation (Fig. 4).

To illustrate the temporal progression of the 3D flow, in Fig. 11 we display velocity isosurfaces for all 18 successive phases of the cycle at Wo = 12. We plot isosurfaces of U_{ax}, where we take as positive (negative) the velocity in the direction of inhalation (exhalation). The positive or negative levels correspond to 50% of the maximum or minimum velocity at each phase. At the beginning of inhalation [Fig. 11(a)], the high-momentum fluid is found mostly along the perimeter of the

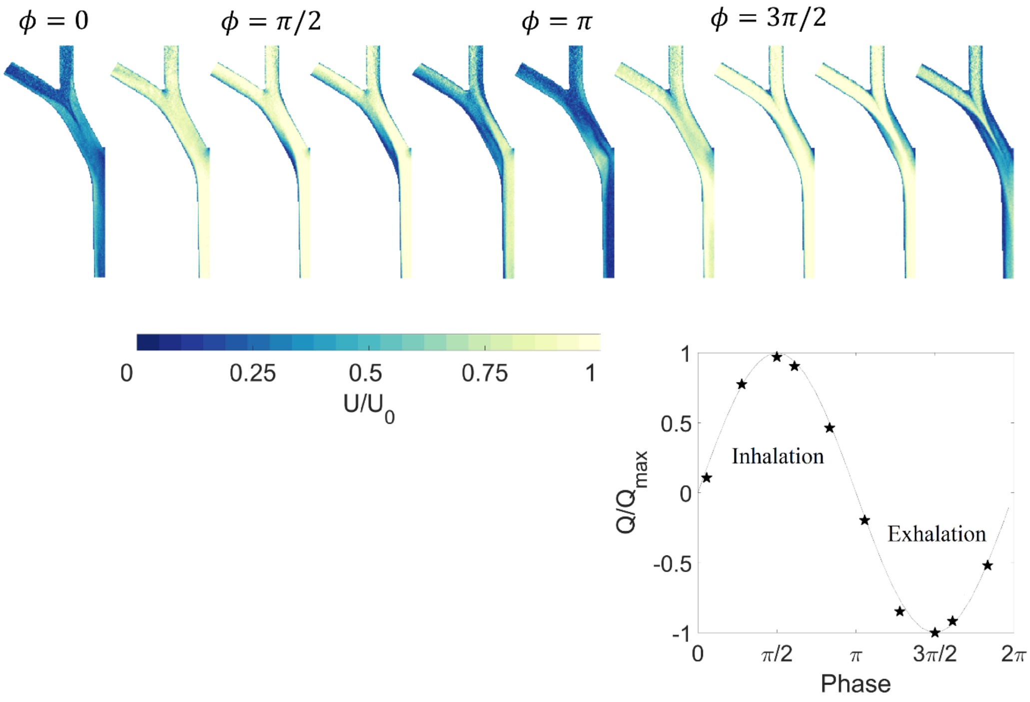

FIG. 10. As Fig. 9, but for the case Wo = 12.

branches, as noted above. Counterflow regions appear along the core of the G_1 branches near the G_1-G_2 junction, and disappear as the inspiratory flow rate increases (b-e). In the deceleration part of inhalation, reverse flow pockets form on the outer side of the G_0-G_1 junction (f) and become larger as the inhalation-to-exhalation inversion is approached (g-i). At the beginning of exhalation (j), the counterflow regions enlarge and dominate the field, with the fast-moving flow (now from G_2 towards G_0) again found near the walls. In this phase, a prominent reverse flow region occupies the central region of the G_0-G_1 junction adjacent to the carina. This recedes as the expiratory flow rate increases, and the high-momentum structures jetting from G_2 into G_1 develop in the second part of exhalation (k-q). Finally, close to the exhalation-inhalation inversion, new counterflow regions (directed in inspiratory direction) form on the lateral sides of G_0 and G_1 (r). These will grow into the dominant flow features seen in the inhalation phase (a), closing the cycle.

The temporal extent of the counterflow regions is noteworthy. As expected, they tend to form close to the inhalation-exhalation and exhalation-inhalation inversions. In both cases, reverse flow pockets are found both along the core of the branch and along the sidewalls. While these regions are short-lived during the exhalation-inhalation inversion (a, r), they last for the entire deceleration part of inhalation and through the inhalation-exhalation inversion (f-j).

A similar analysis for Wo = 6 also reveals the presence of counterflow regions, though these are smaller and primarily confined to the exhalation and inhalation and inhalation and exhalation inversions. These are highlighted in Fig. 12, where the positive or negative isosurface levels correspond to 40% of the maximum or minimum velocity at each phase. Counterflows are hardly visible above the noise floor at Wo = 3, and they are absent at Wo = 1.2.

Past studies have found that forward and reverse flow occupied comparable portions of the bifurcation [27]. Here on the other hand, even at Wo = 12 the reverse flow regions account for a relatively small fraction of the fluid volume. Quantitative discrepancies with previous investigations may be due to multiple factors, including: the bifurcation geometry (for example, in terms of h and θ; see the discussion in Choi [28] on the influence of these parameters); the inflow and

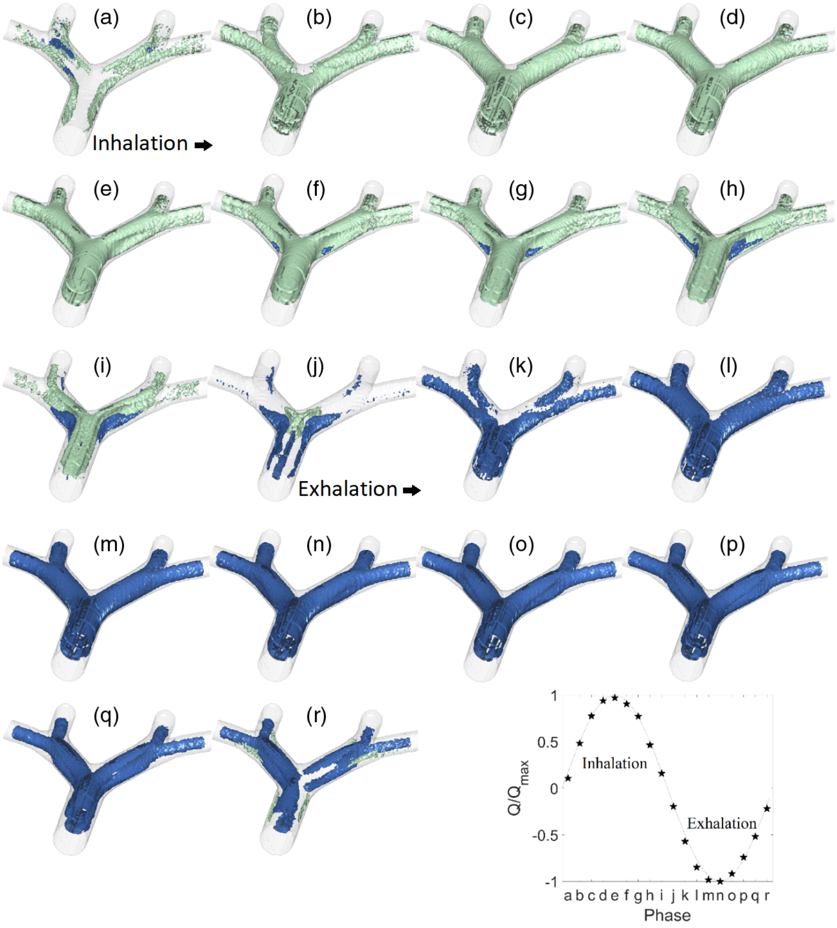

FIG. 11. Velocity isosurfaces for successive phases of the inhalation and exhalation cycle at Wo = 12. Light and dark colors indicate flow moving in the inspiratory and expiratory direction, respectively.

outflow boundary conditions; the Reynolds number; and the presence of successive bifurcations. In particular, we note that most previous studies investigating the presence of counterflow considered single-bifurcation geometries [26–28].

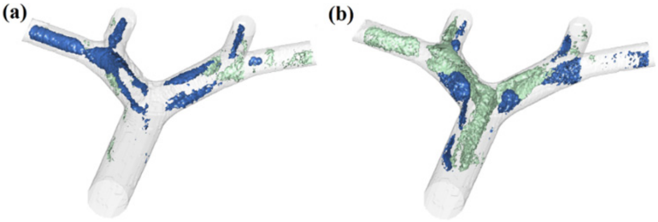

FIG. 12. Velocity isosurfaces at (a) exhalation and inhalation inversion and (b) inhalation and exhalation inversion for the case Wo = 6. Light and dark colors indicate flow moving in inspiratory and expiratory direction, respectively.

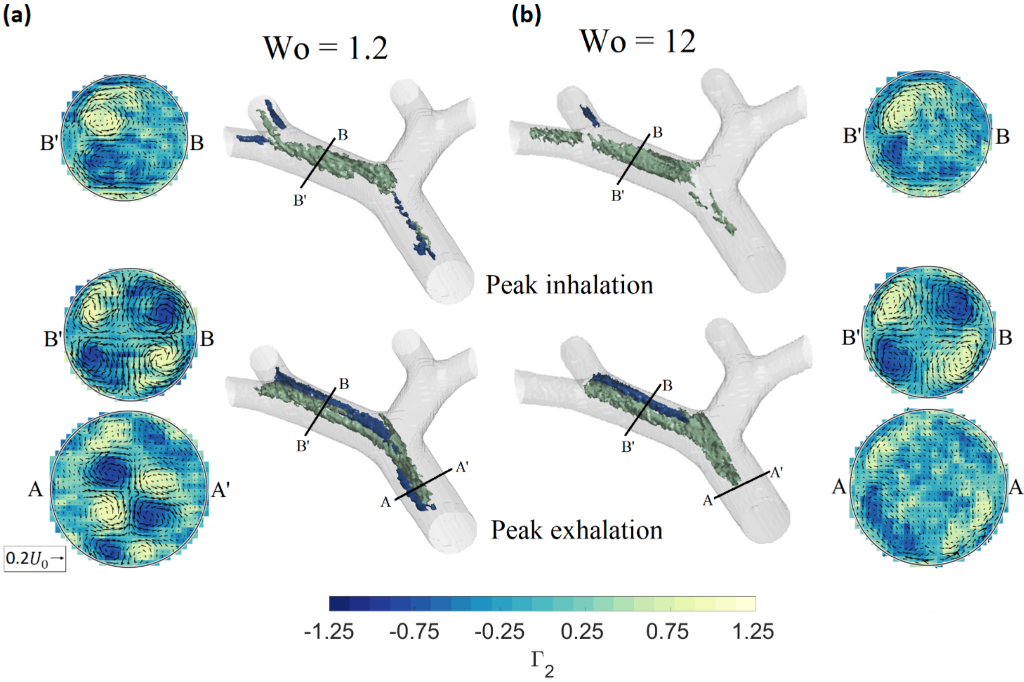

FIG. 13. Γ_2 isosurfaces and cross section contours with in-plane velocity vectors, identifying vortical structures Wo = 1.2 (a) and 12 (b), at peak inhalation and peak exhalation.

2. Secondary flows

We now focus on the time-evolving secondary motions, which we describe using similar quantities as for the steady flow. Figure 13 displays isosurfaces of $\Gamma_2 = \pm 0.45$, as well as cross sections at G_0 and G_1 for the cases Wo = 1.2 and Wo = 12, close to peak inhalation and peak exhalation. The cases Wo = 3 and Wo = 6 (not shown) exhibit qualitatively similar features as Wo = 1.2. At peak inhalation [Figs. 13(a) and 13(b)], independently of Wo, the Dean mechanism generates two counter-rotating vortices at G_1, as seen in the steady inhalation case at the same Re [15]. The spatial resolution in the relatively small granddaughter branches is not sufficient to unequivocally identify the flow structure. However, from the Γ_2 isosurfaces it appears that the counter-rotating vortices in G_1 propagate into the medial G_2 branch, similarly to the steady case; while for the highest Wo the main secondary motions are consistent with a Dean mechanism driven by the local curvature.

At peak exhalation [Figs. 13(c) and 13(d)], G_1 resembles again the steady inspiratory flow, with four counter-rotating vortices present in all investigated Wo cases. On the other hand, the flow in G_0 is very different depending on the oscillatory frequency: at Wo = 1.2 the topology follows the steady exhalation pattern, with a system of multiple counter-rotating vortices propagating from G_1; instead, at Wo = 12 only four vortices are present. The likely reason is that, in the high-frequency case, the core region of the branches is characterized by reduced momentum and thus the vortices located in that area are not advected from G_1 into G_0. Taken together, these results indicate how, at low and intermediate Wo, the secondary flows at peak inhalation and exhalation resemble the steady cases; whereas at high Wo the differences in the momentum distribution are reflected in the transport of streamwise vorticity, and result in different secondary flow structures.

Beside the presence and spatial extent of specific vortical structures, it is of interest to quantify the evolution of the overall secondary flow strength during the oscillatory cycle. Here we focus on G_1, which is the generation least affected from boundary and inflow conditions. Figure 14 plots the

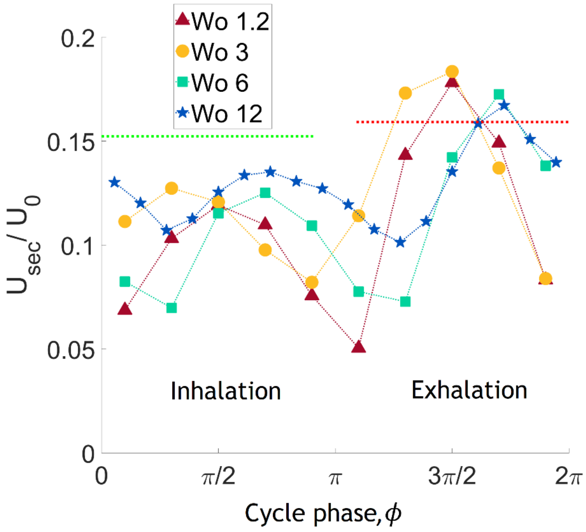

FIG. 14. Time-varying secondary flow strength averaged along G_1, for all considered Wo; the steady inhalation and exhalation levels are also shown for comparison.

secondary velocity (normalized by the peak bulk velocity U_0) averaged along the straight portion of this branch, for all phases and all investigated Wo; the steady inhalation (from Jalal *et al.* [15]) and steady exhalation levels are also shown for comparison. Several observations are in order. The peaks of secondary flow strength are reached close to the phases of maximum flow rate, which is consistent with the fact that the streamwise flow induces the pressure gradients driving secondary motions. The peaks for the higher Wo cases tend to lag those at lower Wo, possibly due to the lag between pressure (and therefore pressure gradients leading to secondary flows) and velocity waveforms at high Wo [20]; however, this effect is hard to quantify due to the limited temporal resolution. The secondary motions are more intense in exhalation than in inhalation, in both steady and oscillatory conditions. This can be explained by the fact that the bulk streamwise velocity decreases along the inspiratory path and increases along the expiratory path; therefore, during exhalation the spatial acceleration acts to augment streamwise vorticity (via the vortex-stretching term in the vorticity transport equation), and vice versa during exhalation. A similar argument was used by Coletti *et al.* [58] to illustrate the stronger and weaker counterrotating vortices formed by a jet issued into a crossflow under favorable or adverse pressure gradient.

The secondary flow strength at peak inhalation is lower compared to the steady case at matching Re, while the opposite is true for peak exhalation. A possible explanation is that the change in secondary flow strength is not symmetric in time, but rather follows a cliff-ramp pattern, as suggested by the curve for Wo = 12. This may result in the temporal acceleration term playing a larger role during the first part of exhalation, when the rate of change of U_{sec} is steeper. The different boundary conditions between the steady cases and the oscillatory ones might also explain, at least in part, the behavior. This point, however, deserves further investigation. Overall, the higher Wo cases display smaller temporal variations of secondary flow strength, and therefore the Wo = 12 case is closer to the steady levels compared to those at lower frequency. In terms of Wo dependence, the conclusion is that (at the considered Re) higher Wo leads to stronger secondary flows during inhalation and weaker secondary flows during exhalation.

3. *Steady streaming*

The measurements of spatially and temporally resolved velocity fields allow us to quantify the phenomenon of steady streaming. At each location, we calculate the streaming (or drift) velocity U_D

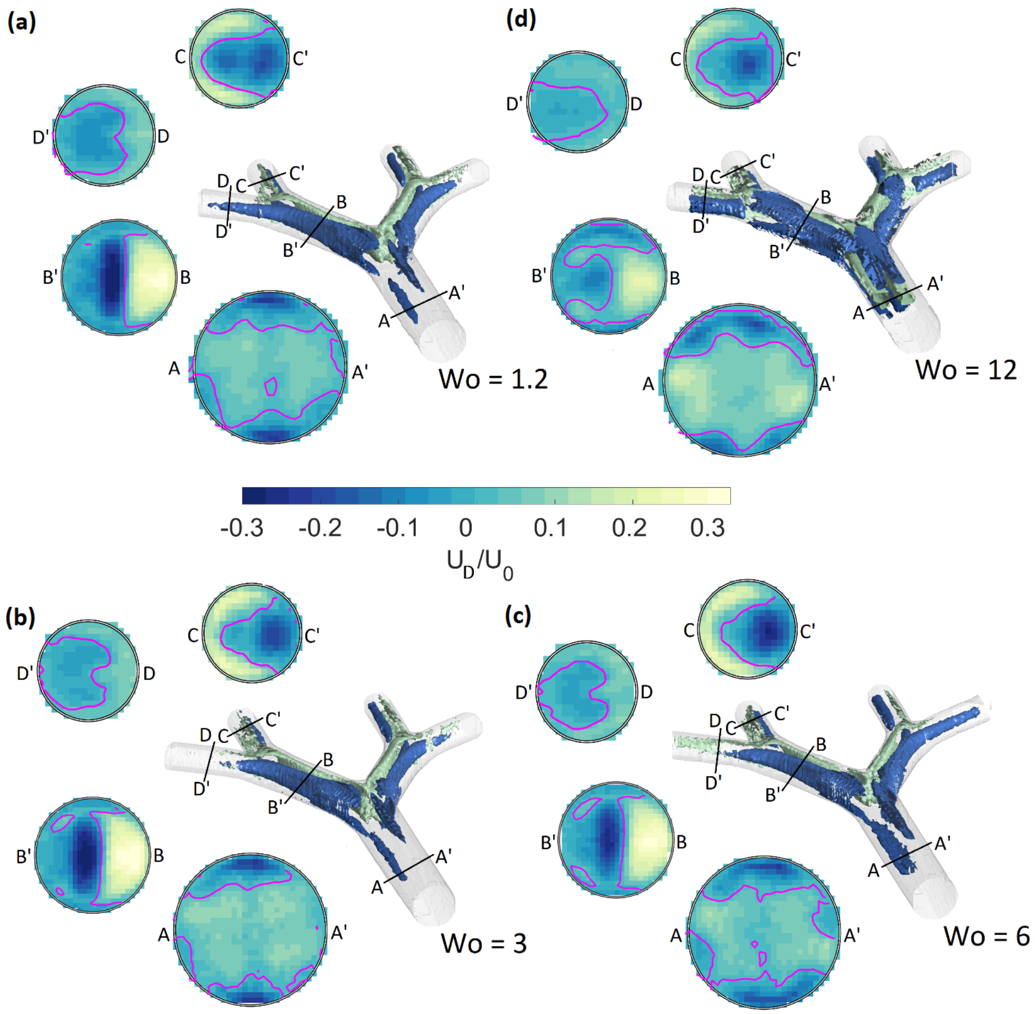

FIG. 15. Isosurfaces and cross section contours of cycle-averaged drift velocity for all considered oscillatory cases Wo = 1.2 (a), Wo = 3 (b), Wo = 6 (c), Wo = 12 (d). Light and dark colors indicate inspiratory and expiratory drift. The purple lines indicate zero drift.

as the cycle-average of the streamwise velocity U_{ax}, thus generating a volumetric field. A similar approach was followed by Peattie and Schwarz [26], who, however, used LDV and reported only a few profiles along the plane of the bifurcation. U_D is taken as positive (negative) when directed in inspiratory (expiratory) direction. In Fig. 15 we display isosurfaces at $U_D = 30\%$ of the maximum or minimum velocity and selected cross sections for all considered Wo cases. At Wo = 1.2, the drift velocities are relatively high in both directions, with peaks of $U_D/U_0 \approx \pm 0.4$ in G_1. (We remark that the inspiratory and expiratory drift need to balance out since the cycle-average over each cross section is zero.) At G_0, most of the cross section sees a weak inspiratory drift, flanked by layers of expiratory drift along the top and bottom sides. This is in contrast with the common picture of steady streaming in the mother branch, where the expiratory drift rather occupies the lateral side of the cross section. This latter type of pattern was obtained in single bifurcations with long mother branches [26,31] and nonplanar multiple bifurcations [29]. The discrepancy with the present results underscores the impact of the geometry and inlet conditions on the drift velocity field. G_1 shows the greatest contrast between inspiratory streaming along the inner part of the bifurcation,

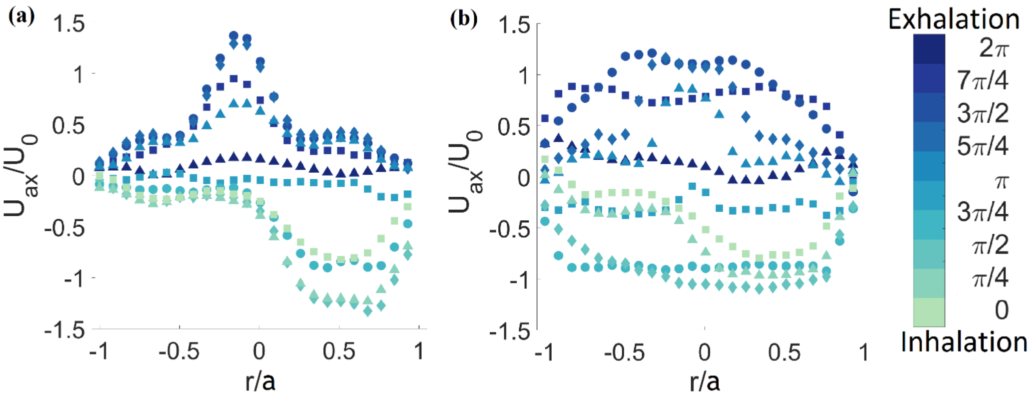

FIG. 16. Streamwise velocity profiles along the bifurcation plane at B-B′ for (a) Wo = 1.2 and (b) Wo = 12, for the different phases in the cycle.

and expiratory streaming over the central and outer part of the branches. This is consistent with the behavior observed during the inhalation and exhalation phases: in the former the high momentum is located close to the carina, while in the latter the merging jets from the granddaughter branches dominate the core of the cross section. A similar drift pattern is visible in G_{2M}, although there the inspiratory drift region wraps around the expiratory drift core. In G_{2L} the steady streaming is negligible.

The U_D fields are qualitatively similar at higher Wo, but the magnitude decreases with increasing ventilation frequency. Overall, the drift velocity is about twice as high at Wo = 1.2 compared to Wo = 12. This can be ascribed to the more skewed streamwise velocity profiles in the low-Wo cases, as compared to the flatter profiles at higher oscillation frequency. Figure 16 quantitatively illustrates this fact by plotting, for several phases, U_{ax} profiles at station B-B′ along the bifurcation plane [the same location of the profiles in Fig. 5(a)], comparing cases Wo = 1.2 and 12. At lower Wo, the inspiratory and expiratory peaks are more pronounced and placed at different locations in the cross section. This sharpens the inhalation and exhalation asymmetry which is at the basis of the steady streaming mechanism [32], and results in larger net transport. Recent simulations from Bauer *et al.* [30] in a double-bifurcation geometry also indicate that the mean square displacement of nondiffusive particles over a given ventilation time decrease with the oscillation frequency. One should remark that Bauer *et al.* kept L/a constant (rather than Re) and therefore a direct comparison with the present data cannot be made.

IV. DISCUSSION AND CONCLUSIONS

We have reported on the flow in a planar double bifurcation model, with proportions and regimes relevant to the central human airways. Expanding on our previous study of steady inhalation in the same geometry [15], the focus has been placed on the steady expiratory flow for a range of Reynolds numbers, and the oscillatory flow for a range of Womersley numbers. As reviewed in the Introduction, this canonical case of Weibel-type bifurcation has been extensively investigated in previous experiments, but always with point-wise or planar techniques. The present volumetric data obtained using MRV provide a comprehensive description of the highly 3D flow topology and allow us to address fundamental open questions.

In comparison with steady inspiration, we confirm that the expiratory flow exhibits flatter velocity profiles, which become progressively blunter in the flow direction. This is mainly due to the redistribution of momentum by the secondary motions, which are stronger in exhalation than in inhalation. The reason for this is twofold. First, at branch bifurcations (where a branch splits in two) the Dean mechanism typically induces two counter-rotation vortices, while at branch junctions (where two branches come together) four vortices are formed. Second, the positive gradient of bulk velocity during exhalation enhances streamwise vorticity, while the opposite occurs during inhalation.

The Reynolds number effect on the expiratory flow topology is conceptually similar as in steady inhalation. At the lower Re, the local geometry primarily determines the flow features: the momentum distribution follows the symmetry of the junctions, and the branch curvature dictates the secondary flow orientation according to the Dean mechanism. This is in keeping with previous experimental studies, that however focused only on relatively low Re (e.g., Fresconi and Prasad [13], who investigated Re $\leqslant 350$). At Re $= 1000$ and higher, on the other hand, the mutual influence of successive junctions is evident in both the axial and secondary velocities. In particular, the streamwise vortices generated at the G_1-G_2 junction have sufficient strength to reach G_0, and radically change the secondary flow pattern. This effect is analogous to the propagation of the inspiratory flow vortices generated at the G_0-G_1 bifurcation, which at Re $= 500$ and above are strong enough to reach G_2 [15]. The determination of the Re level at which this change in topology occurs would require additional measurements, and the precise value will depend on the details of the geometry. We suggest that, in the steady cases, streamwise vortices propagate through successive generations depending on their circulation-based Reynolds number Γ/ν.

In order to evaluate the viability of transport models for biomedical settings, it is important to assess whether steady flow results can be extended to pulsatile conditions. We find that, as long as Wo is in the normal ventilation range (Wo $\leqslant 6$), the phase-averaged 3D flow topology during both inhalation and exhalation phases is similar to the corresponding steady case during most of the ventilation cycle. This is in agreement with previous studies that found steady-like flow structure despite the oscillatory nature of the boundary conditions [29,47]. On the other hand, at Wo levels typical of HFV (Wo $= 12$), the flow structure changes significantly: the acceleration part of both inhalation and exhalation carries the hallmarks of the previous flow inversion, with the high-momentum regions of the flow located close to the walls. Consequently, the secondary motions are also altered, in particular the pattern of counter-rotating streamwise vortices and their ability to propagate across successive generations.

The phenomenon of counterflow is found to be prominent at Wo $= 6$ and 12. Reverse flow pockets are evident during inhalation and inhalation-exhalation inversion, and to a lesser extent during the exhalation-inhalation inversion. Their spatiotemporal extent is smaller compared to what was reported in some previous studies which only addressed single bifurcations; this underscores again the importance of considering multiple bifurcations to capture the mutual influence of adjacent geometric features. The cases at Wo $= 1.2$ and 3 did not show sizeable counterflow. The classification proposed by Jan *et al.* [9], according to which these two cases should have quasisteady behavior (Fig. 2), appears remarkably predictive in this regard.

In both oscillatory and steady conditions, the secondary velocity components are more intense in exhalation than in inhalation. Moreover, their magnitude during inhalation (exhalation) is lower (higher) than in the respective steady cases, with the low-Wo cases showing larger temporal variations during the cycle. Overall, for the considered geometry and Re, the secondary motions during inhalation (exhalation) become stronger (weaker) with increasing Wo. These trends may have important consequences for gas and particle transport, which are both heavily affected by secondary motions [59]. Further research is warranted to ascertain whether such trends are general, or rather specific to the present configuration.

Finally, we have shown that steady streaming, which is often considered a critical mechanism for transport in HFV, is in fact hindered by the flat velocity profiles at high Wo. The drift velocity obtained by cycle averaging the axial velocity is reduced when the ventilation frequency is increased. Therefore, for the same duration of ventilation, HFV may augment the net transport by steady streaming owing to the large number of cycles per unit time, but not as dramatically as it is often assumed. Recent numerical studies [29,30] also point towards a limited role of steady streaming. While studies on more realistic airway geometries are needed to draw firm clinical conclusions, it seems unlikely that the drift velocity per se may explain the efficacy of HFV.

The considered airway model is highly idealized, and therefore this study has not addressed realistic aspects that may significantly influence the respiratory fluid dynamics. A nonexhaustive list includes nonplanarity of the bifurcation tree [11], curvature of the branches [25], larger-than-average branching angles [48], variation of geometric proportions along the tree [50], presence of extra-thoracic airways [60], nonsinusoidal flow waveforms [61], age-dependent changes in flow regime [62], airway wall motion [63], and liquid lining of the bronchi [64]. On the other hand, given the simplified nature of the configuration, the gained insight on fundamental aspects of branching flows is expected to be widely applicable and may be exploited also in other areas such as the cardiovascular circulation.

ACKNOWLEDGMENTS

We gratefully acknowledge the support from the National Science Foundation (Chemical, Bioengineering, Environmental, and Transport Systems, Grant No. 1453538) and the National Institutes of Health (Grants No. NHLBI-R21HL129906 and 1S10OD017974-01).

[1] J. Sznitman, Respiratory microflows in the pulmonary acinus, J. Biomech. **46**, 284 (2013).
[2] B. J. West and A. L. Goldberger, Physiology in fractal dimensions, Am. Sci. **75**, 354 (1987).
[3] E. R. Weibel, Principles and methods for the morphometric study of the lung and other organs, Lab. Invest. **12**, 131 (1963).
[4] T. J. Pedley, Pulmonary fluid dynamics, Annu. Rev. Fluid Mech. **9**, 229 (1977).
[5] C. D. Murray, The physiological principle of minimum work. I. The vascular system and the cost of blood volume, Proc. Natl. Acad. Sci. USA **12**, 207 (1926).
[6] T. A. Wilson, Design of the bronchial tree, Nature (London) **213**, 668 (1967).
[7] B. Sapoval and M. Filoche, Magic trees in mammalians respiration or when evolution selected clever physical systems, Fractals **21**, 1350024 (2013).
[8] Y. Zhao and B. B. Lieber, Steady inspiratory flow in a model symmetric bifurcation, J. Biomech. Eng. **116**, 488 (1994).
[9] D. L. Jan, A. H. Shapiro, and R. D. Kamm, Some features of oscillatory flow in a model bifurcation, J. Appl. Physiol. **67**147 (1989).
[10] J. S. Andrade, Jr., A. M. Alencar, M. P. Almeida, J. Mendes Filho, S. V. Buldyrev, S. Zapperi, and B. Suki, Asymmetric Flow in Symmetric Branched Structures, Phys. Rev. Lett. **81**, 926 (1998).
[11] J. K. Comer, C. Kleinstreuer, and Z. Zhang, Flow structures and particle deposition patterns in double-bifurcation airway models. Part 1. Air flow fields, J. Fluid Mech. **435**, 25 (2001).
[12] B. Mauroy, M. Filoche, E. R. Weibel, and B. Sapoval, An optimal bronchial tree may be dangerous, Nature (London) **427**, 633 (2004).
[13] F. E. Fresconi and A. K. Prasad, Secondary velocity fields in the conducting airways of the human lung, J. Biomech. Eng. **129**, 722 (2007).
[14] T. F. De Vasconcelos, B. Sapoval, J. S. Andrade, Jr., J. B. Grotberg, Y. Hu, and M Filoche, Particle capture into the lung made simple, J. Appl. Physiol. **110**, 1664 (2011).
[15] S. Jalal, A. Nemes, T. Van de Moortele, S. Schmitter, and F. Coletti, Three-dimensional inspiratory flow in a double bifurcation airway model, Exp. Fluids **57**, 148 (2016).
[16] A. Guha, K. Pradhan, and P. K. Halder, Finding order in complexity: A study of the fluid dynamics in a three-dimensional branching network, Phys. Fluids **28**, 123602 (2016).
[17] W. R. Dean, XVI. Note on the motion of fluid in a curved pipe, London Edinburgh Dublin Philos. Mag. J. Sci. **4**, 208 (1927).
[18] R. C. Schroter and M. F. Sudlow, Flow patterns in models of the human bronchial airways, Respiration Physiol. **7**, 341 (1969).
[19] Y. Zhao and B. B. Lieber, Steady expiratory flow in a model symmetric bifurcation, J. Biomech. Eng. **116**, 318 (1994).

[20] Z. Zhang and C. Kleinstreuer, Transient airflow structures and particle transport in a sequentially branching lung airway model, Phys. Fluids (1994–present), **14**, 862 (2002).

[21] C. Kleinstreuer and Z. Zhang, Airflow and particle transport in the human respiratory system, Annu. Rev. Fluid Mech. **42**, 301 (2010).

[22] J. M. Drazen, R. D. Kamm, and A. S. Slutsky, High-frequency ventilation, Physiol. Rev. **64**, 505 (1984).

[23] Y. Imai, S. Nakagawa, Y. Ito, T. Kawano, A. S. Slutsky, and K. Miyasaka, Comparison of lung protection strategies using conventional and high-frequency oscillatory ventilation, J. Appl. Physiol. **91**, 1836 (2001).

[24] J. J. Fredberg, Augmented diffusion in the airways can support pulmonary gas exchange, J. Appl. Physiol. **49**, 232 (1980).

[25] K. Bauer, A. Rudert, and C. Brücker, Three-dimensional flow patterns in the upper human airways, J. Biomech. Eng. **134**, 071006 (2012).

[26] R. A. Peattie and W. Schwarz, Experimental investigation of oscillatory flow through a symmetrically bifurcating tube, J. Biomech. Eng. **120**, 584 (1998).

[27] K. B. Heraty, J. G. Laffey, and N. J. Quinlan, Fluid dynamics of gas exchange in high-frequency oscillatory ventilation: In vitro investigations in idealized and anatomically realistic airway bifurcation models, Ann. Biomed. Eng. **36**, 1856 (2008).

[28] J. Choi *et al.*, Numerical study of high-frequency oscillatory air flow and convective mixing in a CT-based human airway model, Ann. Biomed. Eng. **38**, 3550 (2010).

[29] K. Bauer and C. Brücker, The influence of airway tree geometry and ventilation frequency on airflow distribution, J. Biomech. Eng. **137**, 081001 (2015).

[30] K. Bauer, E. Nof, and J. Sznitman, Revisiting high-frequency oscillatory ventilation *in vitro* and *in silico* in neonatal conductive airway, Clin. Biomech. (2017).

[31] F. R. Haselton and P. W. Scherer, Bronchial bifurcations and respiratory mass transport, Science **208**, 69 (1980).

[32] P. W. Scherer and F. R. Haselton, Convective exchange in oscillatory flow through bronchial-tree models, J. Appl. Physiol. **53**, 1023 (1982).

[33] H. K. Chang, Mechanisms of gas transport during ventilation by high-frequency oscillation, J. Appl. Physiol. **56**, 553 (1984).

[34] J. J. Pillow, High-frequency oscillatory ventilation: Mechanisms of gas exchange and lung mechanics, Crit. Care Med. **33**, S135 (2005).

[35] C. L. Lin, M. H. Tawhai, G. McLennan, and E. A. Hoffman, Characteristics of the turbulent laryngeal jet and its effect on airflow in the human intra-thoracic airways, Respir. Physiol. Neurobiol. **157**, 295 (2007).

[36] S. Miyawaki *et al.*, Effect of carrier gas properties on aerosol distribution in a CT-based human airway numerical model, Ann. Biomed. Eng. **40**, 1495 (2012).

[37] L. Nicolaou and T. A. Zaki, Direct numerical simulations of flow in realistic mouth-throat geometries, J. Aerosol Sci. **57**, 71 (2013).

[38] F. S. Stylianou, J. Sznitman, and S. C. Kassinos, Direct numerical simulation of particle laden flow in a human airway bifurcation model, Int. J. Heat Fluid Flow **61**, 677 (2016).

[39] Y. Liu, R. M. C. So, and C. H. Zhang, Modeling the bifurcating flow in a human lung airway, J. Biomech. **35**, 465 (2002).

[40] Z. Zhang, C. Kleinstreuer, J. F. Donohue, and C. S. Kim, Comparison of micro- and nano-size particle depositions in a human upper airway model, J. Aerosol. Sci. **36**, 211 (2005).

[41] J. A. Bernate *et al.*, Study of the flow unsteadiness in the human airway using large eddy simulation, Phys. Rev. Fluids **2**, 083101 (2017).

[42] S. Discetti and F. Coletti, Volumetric velocimetry for fluid flows, Meas. Sci. Technol. **29**, 042001 (2018).

[43] T. Soodt *et al.*, Analysis of basic flow regimes in a human airway model by stereo-scanning PIV, Exp. Fluids **54**, 1562 (2013).

[44] T. Janke, R. Schwarze, and K. Bauer, Measuring three-dimensional flow structures in the conductive airways using 3D-PTV, Exp. Fluids **58**, 133 (2017).

[45] A. J. Banko *et al.*, Three-dimensional inspiratory flow in the upper and central human airways, Exp. Fluids **56**, 117 (2015).

[46] O. Amili, D. Schiavazzi, S. Moen, B. Jagadeesan, P. F. Van de Moortele, and F. Coletti, Hemodynamics in a giant intracranial aneurysm characterized by in vitro 4D flow MRI, PLoS ONE **13**, e0188323 (2018).

[47] K. Adler and C. Brücker, Dynamic flow in a realistic model of the upper human lung airways, Exp. Fluids **43**, 411 (2007).

[48] A. J. Banko *et al.*, Oscillatory flow in the human airways from the mouth through several bronchial generations, Int. J. Heat Fluid Flow **61**, 45 (2016).

[49] K. Horsfield and G. Cumming, Morphology of the bronchial tree in man, J. Appl. Physiol. **24**, 373 (1968).

[50] T. Van de Moortele, C. H. Wendt, and F. Coletti, Morphological and functional properties of the conducting human airways investigated by in vivo CT and in vitro MRI, J. Appl. Physiol. jap-00490 (2018).

[51] M. Markl, A. Frydrychowicz, S. Kozerke, M. Hope, and O. Wieben, 4D flow MRI, J. Magn. Reson. Imaging **36**, 1015 (2012).

[52] F. G. Hoogenraad, M. B. Hofman, P. J. Pouwels, J. R. Reichenbach, S. A. R. B. Rombouts, and E. M. Haacke, Sub-millimeter fMRI at 1.5 Tesla: Correlation of high resolution with low resolution measurements, J. Magn. Reson. Imaging **9**, 475 (1999).

[53] N. J. Pelc, F. G. Sommer, K. C. Li, T. J. Brosnan, R. J. Herfkens, and D. R. Enzmann, Quantitative magnetic resonance flow imaging, Magn. Resonance Q. **10**, 125 (1994).

[54] A. Padilla, The effect of upstream perturbations on 3D annular diffusers, Ph.D. thesis, Stanford University, 2014.

[55] L. Graftieaux, M. Michard, and N. Grosjean, Combining PIV, POD and vortex identification algorithms for the study of unsteady turbulent swirling flows, Meas. Sci. Technol. **12**, 1422 (2001).

[56] J. C. R. Hunt, S. Leibovich, and K. J. Richards, Turbulent shear flows over low hills, Q. J. R. Meteorol. Soc. **114**, 1435 (1988).

[57] J. R. Womersley, Method for the calculation of velocity, rate of flow and viscous drag in arteries when the pressure gradient is known, J. Physiol. **127**, 553 (1955).

[58] F. Coletti, C. J. Elkins, and J. K. Eaton, An inclined jet in crossflow under the effect of streamwise pressure gradients, Exp. Fluids **54**, 1589 (2013).

[59] C. Kleinstreuer, Z. Zhang, and J. F. Donohue, Targeted drug-aerosol delivery in the human respiratory system, Annu. Rev. Biomed. Eng. **10**, 195 (2008).

[60] J. Choi, M. Tawhai, E. Hoffman, and C. Lin, On intra-and intersubject variabilities of airflow in the human lungs, Phys. Fluids **21**, 101901 (2009).

[61] M. Alzahrany, A. Banerjee, and G. Salzman, Flow transport and gas mixing during invasive high frequency oscillatory ventilation, Med. Eng. Phys. **36**, 647 (2014).

[62] J. M. Oakes, S. C. Roth, and S. C. Shadden, Airflow simulations in infant, child, and adult pulmonary conducting airways, Ann. Biomed. Eng. **46**, 498 (2018).

[63] W. A. Wall and T. Rabczuk, Fluid-structure interaction in lower airways of CT-based lung geometries, Int. J. Numer. Methods Fluids **57**, 653 (2008).

[64] J. B. Grotberg, Respiratory fluid mechanics and transport processes, Ann. Biomed. Eng. **3**, 421 (2001).